High Temperature Corrosion of Materials (2024) 101:755–778
https://doi.org/10.1007/s11085-024-10243-0

ORIGINAL PAPER

Oxidation Behavior of $Al_xHfNbTiVY_{0.05}$ Refractory High-Entropy Alloys at 700–900 °C

Fadhli Muhammad[1,2,3] · **Dmitry Sukhomlinov**[3] · **Lassi Klemettinen**[3] · **David Sibarani**[3] · **Eddy Agus Basuki**[2] · **Daniel Lindberg**[3] · **Pekka Taskinen**[3] · **Akhmad Ardian Korda**[2] · **Zulfiadi Zulhan**[2] · **Djoko Hadi Prajitno**[4]

Received: 6 November 2023 / Revised: 5 March 2024 / Accepted: 19 March 2024 /
Published online: 16 April 2024

Abstract

Refractory high-entropy alloys (RHEA) are considered as potential candidates for new-generation energy-related high-temperature applications. However, the poor high-temperature oxidation resistance of RHEAs, resulting in phenomena such as significant weight gain, scale spallation, pesting, and even complete oxidation, limits their applications. In this study, the oxidation behavior of $Al_xHfNbTiVY_{0.05}$ ($x = 0.75$; 1; 1.25) high-entropy alloys was investigated at 700–900 °C. The isothermal oxidation tests showed that the oxidation resistance of $Al_xHfNbTiVY_{0.05}$ RHEA is strongly influenced by temperature and time. In addition, accelerated oxidation, known as pesting, was observed to occur at 700 °C for all alloys; while, partial spallation was observed at 800 °C for the Al_1 and $Al_{1.25}$ alloys. Detailed analyses of oxidation kinetics have been carried out for the oxidation test series at 900 °C. The mechanism behind disintegration was investigated and attributed to accelerated internal oxidation followed by the formation of voluminous Nb_2O_5, $TiNb_2O_7$, and fast-growing $AlNbO_4$, and is also thought to be related to the partial evaporation of V_2O_5.

Keywords Refractory high-entropy alloys · Corrosion · Accelerated oxidation · Pesting

Introduction

The thrust-to-weight ratio and fuel efficiency will continue to improve as high-power turbine engine technology evolves. Following the basic principles of jet propulsion, fuel consumption depends on fuel energy, engine thrust, thermal

Extended author information available on the last page of the article

Table 1 Room temperature properties of RHEAs as reported in the literature

Alloy system	ρ (g/cm^3)	Phase	σ_{ys} (MPa)	ε_f (%)	Refs.
HfNbTaTiZr (Compression)	9.89	BCC	929	~ 10	8
NbTiVZr (Compression)	6.43	BCC + BCC	1105	–	11
HfNbTiZr (Tensile)	8.23	BCC	879	~ 15	12
HfNbTiV (Tensile)	–	BCC	1004	~ 16.1	13
$Hf_{24}Nb_{23}Ti_{38}V_{15}$ (Tensile)	–	BCC	774	~ 20.6	13

ρ, σ_{ys}, and ε_f represent density, yield strength, and fracture elongation for the mentioned RHEAs

efficiency, and engine weight. As the turbine inlet temperature increases, the power output of the high-pressure turbine engine increases [1, 2]. Of all the known alloys, Ni-based superalloys have the best combination of the required properties, including creep resistance, temperature stability, environmental resistance, and damage tolerance. Today, operating temperatures, particularly during takeoff, are approaching or exceeding the theoretical limits of these materials, i.e., 1150 °C due to their inherent melting points [3]. The current solution to this material problem is to implement active or passive cooling systems and thermal barrier coatings (TBCs), which have enabled a remarkable increase in turbine performance. Due to the difficulty in achieving the required combination of properties, in particular toughness and resistance to foreign object damage, numerous attempts to move beyond superalloys by investigating alternatives such as ceramics and intermetallics have been conducted but with little success [1, 4]. It is therefore necessary to explore new high-temperature alloys that are superior to the current Ni-based superalloys.

Using the ideas of Yeh et al. [5] for high-entropy alloys (HEAs) and Cantor et al. [6] for equiatomic multicomponent alloys, Senkov et al. [7, 8] developed a new class of alloys called refractory high-entropy alloys (RHEAs). RHEAs are characterized by high melting points and some of them have outstanding thermal stability at elevated temperatures. Because of these factors, the development of RHEAs is expected to find new applications in extreme environments. The MoNbTaW and MoNbTaVW RHEAs were reported in 2010 by Senkov et al. [7, 9]. Later, other alloy systems such as HfNbTaTiZr [8] and $CrMo_{0.5}NbTa_{0.5}TiZr$ [10] were investigated. However, all these alloys exhibited extreme brittleness at room temperature. So far, only a few alloy systems such as HfNbTaTiZr [8], NbTiVZr [11], HfNbTiZr [12], and HfNbTiV [13] have been shown to have sufficient properties at room temperature, as shown in Table 1.

It is well-known that refractory elements and their alloys are limited by poor high-temperature oxidation resistance, and RHEAs are no exception [14]. To improve the oxidation resistance, Al, Cr, and Si have been added to form protective scales such as Al_2O_3, Cr_2O_3, and SiO_2. The addition of these non-refractory metals seems to be a promising method to improve high-temperatures oxidation resistance [3, 14–18]. However, the addition of Al, Cr, and Si to RHEA increases the chance of forming unwanted intermetallics (e.g., Nb_5Si_3, $NbCr_2$, $MoSi_2$, and Nb_3Al) and causing embrittlement [19]. Moreover, the addition of alloying elements such as Al, Cr, and Si into Zr or Hf-containing alloys has a limited effect due to the formation of ZrO_2 and HfO_2, which are thermodynamically more favorable compared to Al_2O_3, Cr_2O_3, and SiO_2.

Pesting, which means a rapid disintegration of the metallic substrate due to intergranular oxidation, is an unusual process that can happen at moderate temperatures of 600–800 °C [14, 20]. According to Sheikh et al. [21], the failure in forming protective oxide scales and the accelerated internal oxidation are the pesting mechanisms in $Hf_{0.5}Nb_{0.5}Ta_{0.5}Ti_{1.5}Zr$ RHEA. The pesting phenomenon in this alloy can be eliminated by removing Zr and Hf simultaneously. Chang et al. [22] revealed that the formation of mixed oxides in the oxide scale and its low-density structure are responsible for the pesting that occurred in HfNbTaTiZr RHEA. Although the protection is not as good as that by a dense alumina layer, the addition of Al to the alloy substantially enhances the oxidation resistance and inhibits pesting. It is expected that the slight difference in the heat of formation between aluminum oxide and other oxides causes the formation of a mixed oxide layer that contains alumina. This alumina containing mixed oxide provides essential protection and thus a higher Al content provides a thicker mixed oxide scale. Wei et al. [13] compared the oxidation behaviors of $Ti_{38}V_{15}Nb_{23}Hf_{24}$ and $Ti_{25}V_{25}Nb_{25}Hf_{25}$ RHEAs at 600, 800, and 1000 °C, and verified that drastic catastrophic oxidation occurs in the $Ti_{25}V_{25}Nb_{25}Hf_{25}$ RHEA due to the site-preferential oxidation of Ti and Nb occurring at grain boundaries. A more decent oxide scale formed on the surface of $Ti_{38}V_{15}Nb_{23}Hf_{24}$ RHEA and no pest oxidation or spallation was detected. Ouyang et al. [23] reported two different oxidation behaviors in $Ti_{38}V_{15}Nb_{23}Hf_{24}$ RHEA. A dense composite oxide layer was formed on the surface of RHEA at temperatures below 1000 °C. This layer has a consistent lattice constant and crystallographic orientation; while, internal oxidation with the formation of needle-like HfO_2 occurred in the alloy matrix below the alloy–oxide scale interface at temperatures above 1000 °C. The internal oxidation was attributed to the sufficient inward diffusing oxygen after decomposition of the dense outer oxide layer with sluggish oxygen diffusivity.

To date, most research efforts have focused on oxidation behavior at extremely high temperatures ignoring oxidation resistance at intermediate temperatures between 500 and 800 °C, where pesting is likely to occur in RHEA. There are only two articles describing detailed cases of pesting in RHEA [21, 22], indicating the scarce knowledge of pesting in RHEAs. Therefore, this work attempts to identify the temperature range in which pesting is most likely to occur in one of the RHEAs, the $Al_xHfNbTiV$ system. The oxidation behavior and microstructure of the oxide layer of Y-doped $Al_xHfNbTiV$ RHEAs, where x varies from 0.75 to 1.25, were investigated in this work.

Experimental Procedures

Sample Preparation

The primary alloys of $Al_xHfNbTiV$ doped with Y (1 at%) ($x = 0.75$; 1; 1.25) were prepared using high purity metals (> 99.9%) by arc melting in a water-cooled copper mold under a high purity argon (99.99%) atmosphere. Three model alloys were designated $Al_{0.75}$, Al_1, and $Al_{1.25}$. Each prepared ingot was turned and remelted at least five times to ensure alloy homogenization. The detailed synthesis of the alloys has been the subject of a previous study [24]. The ingots were cut into small cuboids using a low speed diamond cutter. The samples were then sequentially ground on 400, 600, 1200, and 1500 grit silicon carbide abrasive papers and ultrasonically cleaned in ethanol for 10 min. The final samples with dimensions of 7 mm × 6 mm × 5 mm and an average weight of 1.5 g were prepared for oxidation tests.

Oxidation Tests

Oxidation tests were performed in a split horizontal quartz tube furnace (Lenton CSC 12/600H, UK) in dry air with a flow rate of 223 mL/min. The flow rate was controlled by a DFC26 digital mass flow controller (Aalborg, USA). Temperature in the furnace tube was measured with a calibrated S-type Pt/Pt-10 wt% Rh thermocouple (Johnson-Matthey Noble Metals, UK) at the sample location and connected to a 2010 DMM multimeter (Keithley, USA). The furnace was preheated to the oxidation temperature of 700, 800, or 900 °C at a heating rate of 4 °C/min, and the exposure times were set at 1, 4, 9, 16, and 25 h for each temperature. The samples were placed in an alumina boat and positioned in the hot zone when the target temperature was reached with an accuracy of ± 2 °C and removed from the furnace to cool in air after the desired exposure time was reached. The samples were weighed using an analytical balance to an accuracy of 0.1 mg. It should be noted that only the bulk samples were weighed, without taking into account the spalled powders. This is because the severity of pesting or powder spallation is an interesting and highlighted focus in this study. One sample was used for each oxidation test.

Characterization of Oxidation and Microstructure

The cross sections of the oxidized specimens were mounted in epoxy, ground, and polished with diamond suspensions to 3 μm and then 1 μm using metallographic polishing cloths. Samples were not etched. The microstructure and surface morphology of the samples were examined using a MIRA 3 scanning electron microscope (SEM; Tescan, Brno, Czech Republic) equipped with an UltraDry Silicon Drift energy dispersive X-ray spectrometer (EDS; Thermo Fisher Scientific, Waltham, MA, USA). The SEM was operated at acceleration voltage of 15 kV and beam current between 10 and 11 nA on the sample surface during imaging and EDS analysis (for point analysis, area analysis, and elemental mapping). The standards used for the concentration quantifications are listed in Table 2. The phase constituents of the oxidation products (spalled powder) were characterized using an X'PERT PRO MPD Alpha 1 X-ray diffractometer (XRD; PANalytical, Almelo, The Netherlands) with Cu-Kα radiation ($\lambda = 0.154$ nm) operating at 40 kV and 40 mA in the 2θ scattering range

Table 2 Standards used in EDS analyses for concentration quantifications

Element	X-ray line analyzed and standard material used
O	Kα, diopside
Al	Kα, aluminum
Ti	Kα, titanium
V	Kα, vanadium
Y	Lα, yttrium
Nb	Lα, niobium
Hf	Lα, hafnium

between 15 and 80° and step length 0.0263°. The XRD patterns were analyzed using ICDD PDF 4 and Match! Software.

Equilibrium Calculations

Thermodynamic calculations were performed using commercial FactSage 8.2 software (FactSage™, Thermfact and GTT-Technologies). The calculations presented originate from the FactPS database in combination with the FToxid database [25].

Results

Alloy Microstructure

The microstructures of the as-cast $Al_{0.75}$, Al_1, and $Al_{1.25}$ alloys have been described in detail previously [24]. The $Al_{0.75}$ alloy has a single-phase BCC structure with no secondary phases; while, the Al_1 and $Al_{1.25}$ alloys have BCC structures with multiple phases that contain (Ti, Nb)Al_2 precipitates or AB_2-type intermetallic compounds, with Ti and Nb serving as element A and Al as element B. All alloys have excellent room-temperature hardness as compared to previously reported HEAs and commercial Ni-based superalloys [26, 27].

General Oxidation Behavior

The weight change per unit area versus time curves for the oxidized RHEA in the temperature range of 700–900 °C are shown in Fig. 1. Three different oxidation responses were observed. At 700 °C, all RHEA samples showed accelerated oxidation as evidenced by the gradual disintegration of the material into powder, while at 800 and 900 °C, the alloys showed different responses ranging from moderate to severe oxidation with noticeable spallation in some alloys at 800 °C, and bulky oxide formation in all alloys at 900 °C. The oxidation behavior is generally classified

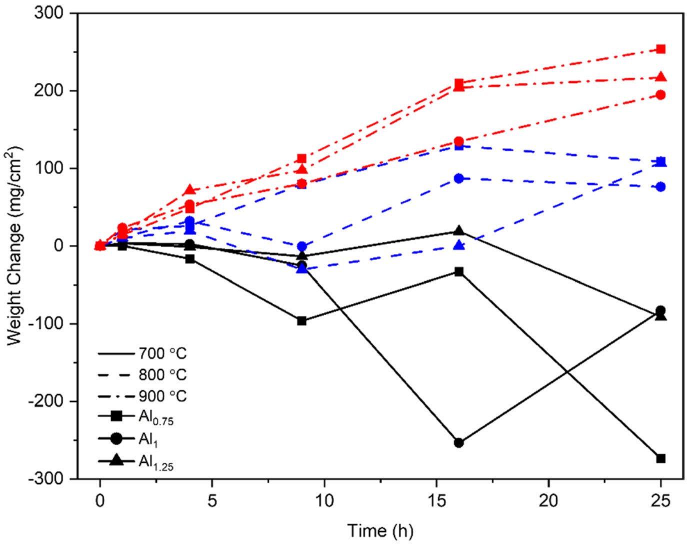

Fig. 1 Weight change (only the bulk alloy was weighed, excluding the fine spalled-off powders) as a function of exposure time

according to whether the metal underwent pesting or bulky oxide formation. In the first case, continuous weight loss (only the bulk sample was weighed, excluding the spalled powders) was observed in almost all model alloys at 700 °C.

Continuous spallation from the sample surface, known as pesting, exposes fresh surfaces to oxidation and eventually causes the alloys to disintegrate into powder. Similar behavior has been observed in conventional refractory intermetallics, such as $NbAl_3$ and $MoSi_2$ [28–34]. In this work, pesting was more severe for the $Al_{0.75}$ than for the other alloys at 700 °C, with a significant weight change of -273 mg/cm^2 after 25 h.

Noticeably, there was a very slight initial positive weight gain, although insignificant on the graph, for oxidation at 700 °C for the Al_1 alloy for up to 4 h. However, further exposure resulted in a negative weight change, and a significant weight loss occurred after 16 h. Spallation was observed in all alloys after 9 h of oxidation, with the Al_1 alloys showing progressively greater weight loss after 16 h, in contrast to the $Al_{0.75}$ and $Al_{1.25}$ alloys, where the weight change was less negative than the previous exposure time.

A continuous weight gain occurred for all the model alloys at 900 °C, indicating that they followed the power law as shown in Fig. 2; whereas, the oxidation curves were fitted with the oxidation growth law:

$$\Delta m = kt^n \tag{1}$$

where Δm is the weight gain per unit surface area, t is the exposure time (in seconds), k is the rate constant, and n is the empirical time exponent used to distinguish the processes limiting oxide growth. The empirical exponents obtained are tabulated in Table 3, where the n values closer to 1 and 0.5 represent near-linear

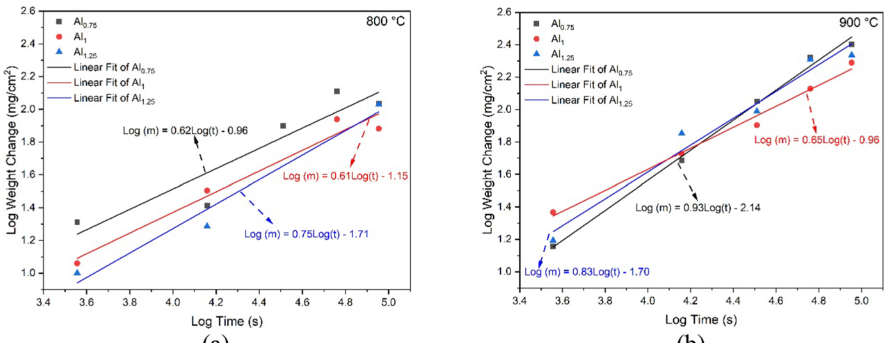

Fig. 2 Fitted lines of the oxidation weight gain data of $Al_xHfNbTiVY_{0.05}$ RHEAs at **a** 800 °C and **b** 900 °C

Table 3 Fitting data of k and n values for $Al_xHfNbTiVY_{0.05}$ RHEAs in the exposure of air at 800 and 900 °C

ID	800 °C		900 °C	
	k, $g^2/cm^4\ s^{2n}$ (0–25 h)	n	k, $g^2/cm^4\ s^{2n}$ (0–25 h)	n
$Al_{0.75}$	7.9×10^{-10}	0.62	2.5×10^{-11}	0.93
Al_1	1.5×10^{-10}	0.61	1.1×10^{-9}	0.65
$Al_{1.25}$	2.7×10^{-11}	0.75	8.2×10^{-11}	0.83

and near-parabolic oxidation kinetics, respectively. The evaluation of the weight gain data at 800–900 °C showed that the weights of the alloys exhibited a variety of growth rates, ranging from near-linear to near-parabolic growth rates.

The presence of yellowish matter on the surface of the quartz tube at the end of the furnace (where temperature was lower) was expected to be condensation products of volatile V_2O_5 oxides. The yellowish matter has also been reported and attributed to the formation of molten V_2O_5 in the case of Ti–6Al–4V was exposed to oxidizing environments at elevated temperatures [35, 36]. However, the XRD patterns, as shown in Fig. 3, indicated that a wide range of oxides (Nb_2O_5, $AlNbO_4$, TiO_2, HfO_2, and HfV_2O_7) were the predominant oxidation products after oxidation at 700 °C, where no V_2O_5 oxides were found. Still, it should be noted that their similarity and the enormous number of high-to-low intensity peaks that could not be attributed to any recognized phase made it more difficult to distinguish between multiple peaks/phases.

Microstructural and Compositional Analysis

Cross Section Analysis at 700 °C

The formation of oxidation products was investigated using microscopy and equilibrium calculations. Figures 4, 5, and 6 show the cross sections of the oxidation

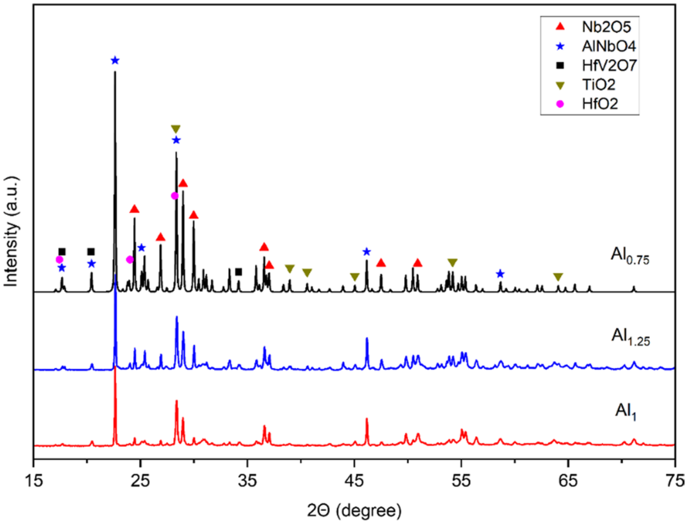

Fig. 3 XRD patterns of the spalled powder and yellowish powder post-oxidation at 700 °C

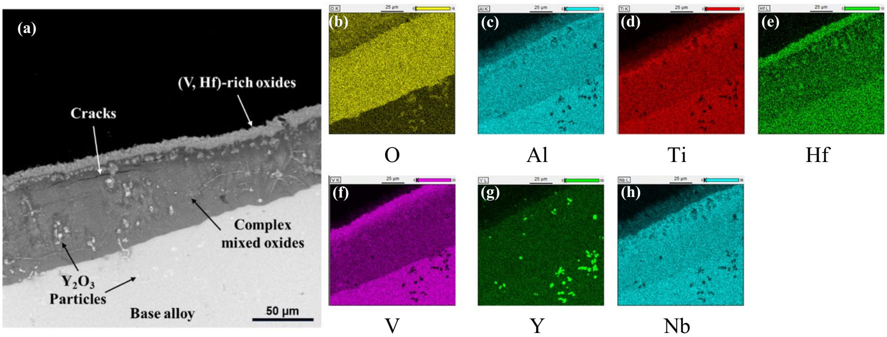

Fig. 4 Microstructure of a cross section for $Al_{0.75}$ alloy oxidized at 700 °C for 9 h (**a**); EDS element mapping results are shown in (**b**–**h**), V and Hf are enriched in the outermost oxide scale as indicated by arrows

scales formed on the surface of the samples after exposure at 700 °C. Figure 4 shows that the $Al_{0.75}$ alloy contains two layers of oxides: the thin (~10 μm) outer oxide layer and the thick inner oxide layer. The outer layer has a porous structure consisting of (V and Hf)-rich oxides, and the inner layer has a denser structure consisting of (Al, Nb, Ti)-rich oxides. Cracks were observed at the interface between inner and outer layers. In addition, Y_2O_3 oxide was observed in both the oxide layer and the base alloy. Figures 5 and 6 show the unprotective oxide layers on the surface of the Al_1 and $Al_{1.25}$ alloys, respectively. The alloys exhibit continuous oxidation which eventually leads to complete disintegration. There is no evidence of protective behavior observed even in the initial oxidation period,

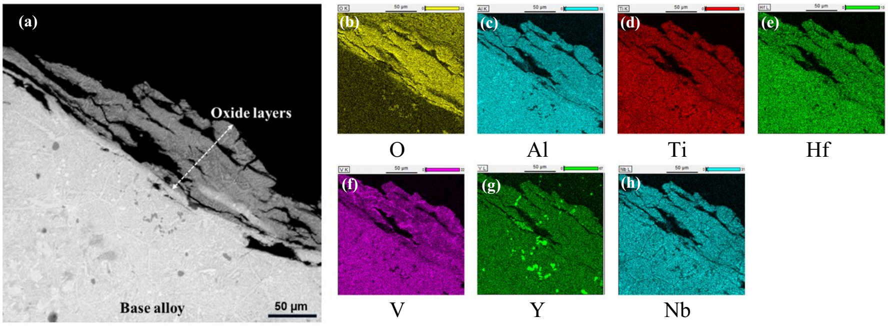

Fig. 5 Microstructure of the Al_1 alloy cross section oxidized at 700 °C for 16 h (**a**); EDS element mapping results are shown in (**b**–**h**)

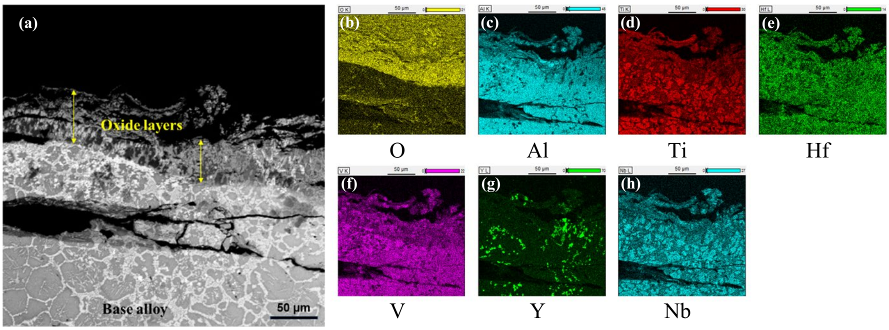

Fig. 6 Microstructure of the $Al_{1.25}$ alloy cross section oxidized at 700 °C for 9 h (**a**); EDS element mapping results are shown in (**b**–**h**)

as shown in Fig. 1. Cracks developed in some regions, mostly in oxide scales, due to the formation of higher oxides from MO-type oxides. Stresses generated in the oxides by the mismatch in volumetric dimensions accumulate and are released by cracking as the oxides grow.

Figure 7 shows the calculated oxide scale stability diagram of the $Al_xHfNbTiVY_{0.05}$ RHEA system as a function of temperature. The results agree fairly well with the post-oxidation analysis, which shows that the oxide layers formed at 700 °C are composed of mixed complex oxides HfO_2, corundum-type $(Al, V)_2O_3$, Nb_2O_5, TiO_2 (rutile), V_2O_5 (in liquid form), and Y_2O_3.

Cross Section Analysis at 800 °C

At 800 °C, the oxide scales appear to have developed for all alloys. Some slight protective behavior appears, although pesting and/or partial spallation still occurred in the Al_1 and $Al_{1.25}$ alloys. The $Al_{0.75}$ shows minor pesting behavior but generally exhibits gradual weight gain. Figures 8, 9, and 10 show the developed cross section

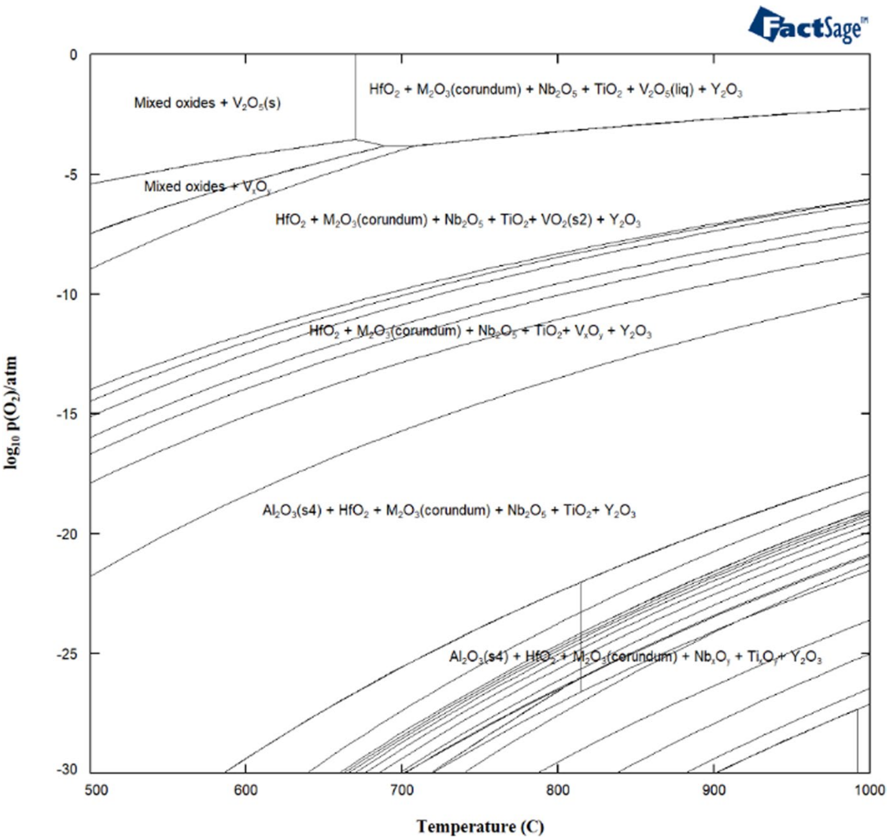

Fig. 7 Calculated oxide scale stability diagram of the $Al_xHfNbTiVY_{0.05}$ RHEA system as a function of temperature (by FactSage 8.2, using FactPS and FToxid databases)

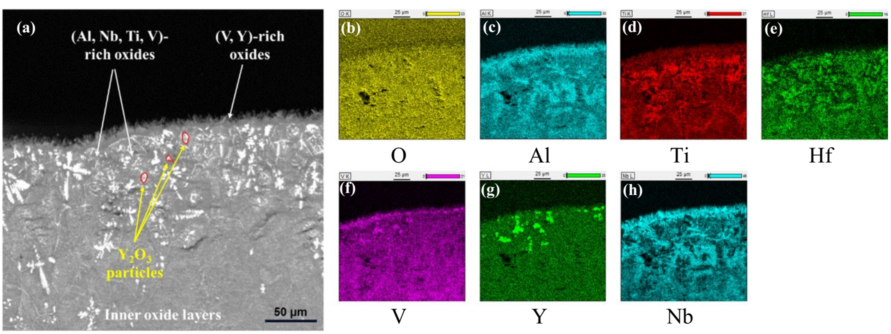

Fig. 8 Microstructure of the $Al_{0.75}$ alloy cross section oxidized at 800 °C for 9 h (**a**); EDS element mapping results are shown in (**b**–**h**)

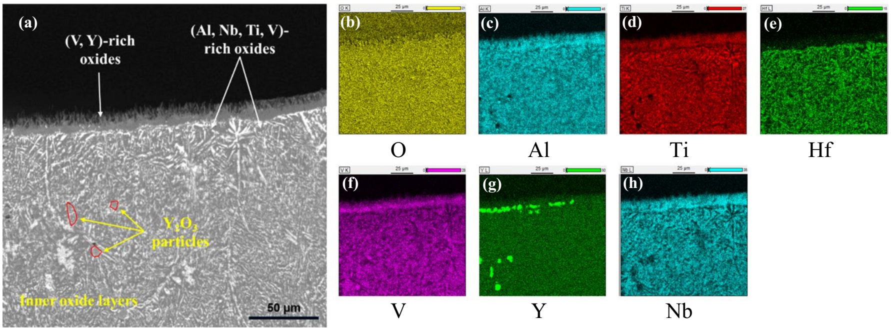

Fig. 9 Microstructure of the Al_1 alloy cross section oxidized at 800 °C for 9 h (**a**); EDS element maps are shown in (**b–h**), V and Y are enriched at the needle-like oxide structure

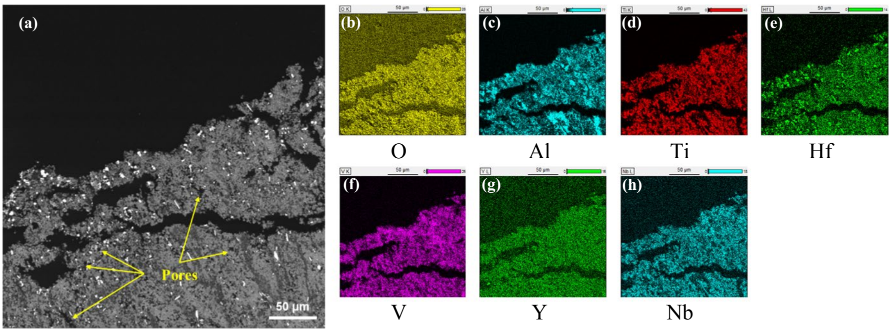

Fig. 10 Microstructure of the $Al_{1.25}$ alloy cross section oxidized at 800 °C for 9 h (**a**); EDS element maps are shown in (**b–h**)

of the oxidation layer formed on all the samples at 800 °C. As shown in Figs. 8 and 9, both $Al_{0.75}$ and Al_1 alloys show similar oxide layers with the formation of two distinct scales. The outer thin layer has a needle-like structure composed of (V, Y)-rich oxide particles and the inner thick layer is composed of (Al, Nb, V, Ti)-rich oxides. The oxide morphologies for both alloys are similar to the oxide morphology found in the $AlNbTiVZr_{0.25}$ alloy after oxidation at 800 °C for 100 h [37]. The $Al_{1.25}$ alloy, however, has a single thick oxide layer with a loose, voluminous oxide structure, as shown in Fig. 10. Such a structure cannot prevent both inward diffusion of oxygen from air and outward diffusion of metallic cations, resulting in continuous oxidation which gradually leads to the disintegration of the bulk material.

Cross Section Analysis at 900 °C

At 900 °C, the development of oxide scales still occurred in all alloys. The pesting and spalling behavior was not observed in the alloys. Figure 11, 12, 13, and 14 show the surface morphology of all alloys oxidized at 900 °C for 9 h. Figure 11 shows the

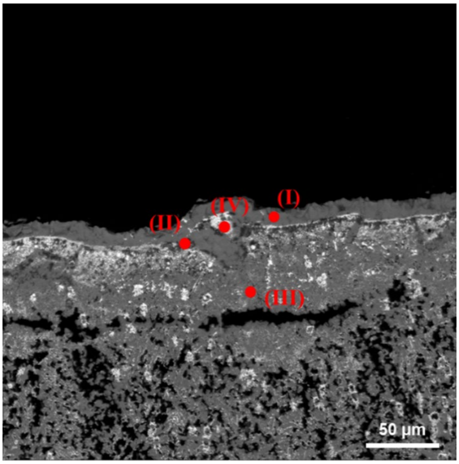

Fig. 11 Backscattered electron image of the upper oxidation layer of $Al_{0.75}$ alloy after 9 h exposure in dry air at 900 °C (the point analyses are shown in Table 4)

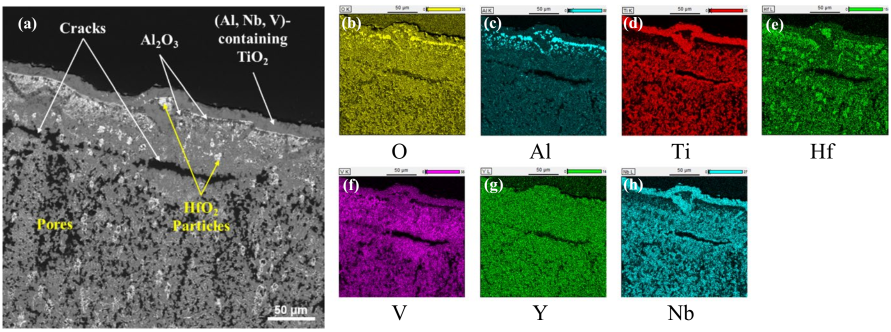

Fig. 12 Microstructure of the $Al_{0.75}$ alloy cross section oxidized at 900 °C for 9 h (**a**); EDS element mapping results are shown in (**b–h**). Al, Ti, and V are noted to be enriched at the outermost oxide layer as indicated by arrows

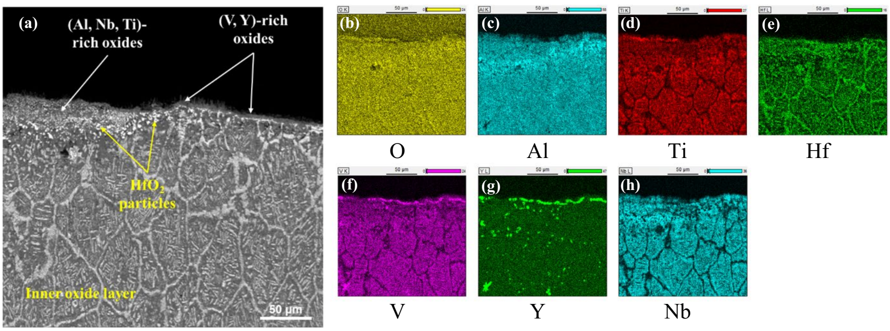

Fig. 13 Microstructure of the Al_1 alloy cross section oxidized at 900 °C for 9 h (**a**); EDS element mapping results are shown in (**b–h**). V and Y are noted to be enriched in the needle-like structure

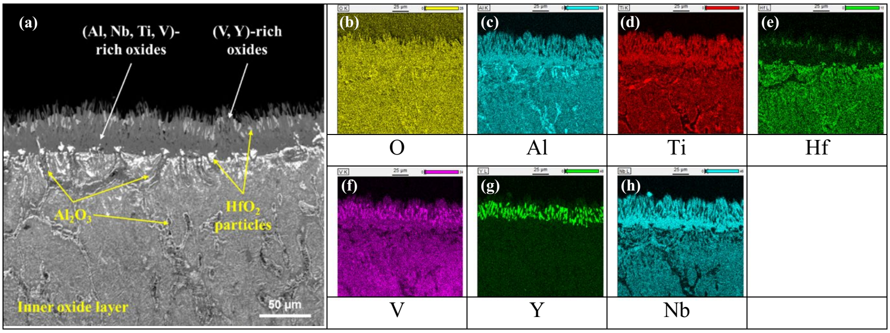

Fig. 14 Microstructure of the $Al_{1.25}$ alloy cross section for oxidized at 900 °C for 9 h (**a**); EDS element mapping results are shown in (**b**–**h**).V and Y are noted to be enriched in the needle-like structure

Table 4 EDS point analyses in the cross section of the $Al_{0.75}$ alloy oxidized at 900 °C for 9 h, in selected regions shown in Fig. 11

Composition	Element (at %)						
Point	Al	Hf	Nb	Ti	V	Y	O
(I)	5.18	2.05	5.96	28.71	8.42	0.01	51.89
(II)	36.67	3.30	0.07	0.64	4.02	0.11	55.20
(III)	5.83	2.83	4.68	24.36	13.00	0.06	49.25
(IV)	5.36	31.59	0.86	1.71	14.22	1.02	45.24

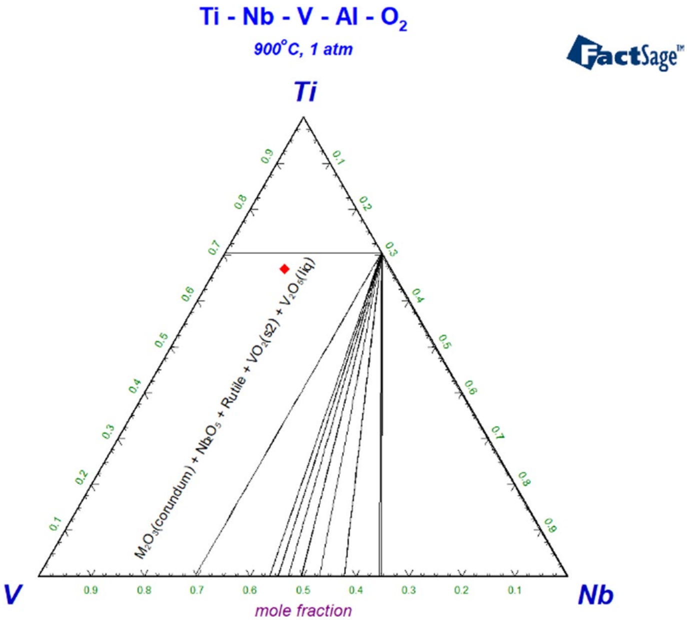

Fig. 15 A section of the quinary phase diagram for the Ti–Nb–V–Al–O_2 system at 900 °C illustrates the stable oxides stability domains obtained using the FactSage 8.2 (FactPS and FToxid databases). Point (I) is denoted with a red dot, in accordance with the data from Table 4

formation of two oxide scales: the outer thin layer (~15 μm) appears to be denser/less porous than the inner, thicker layer. EDS analysis shows that the outer layer is composed of (Al, Nb, V)-containing TiO_2, and the inner layer of (Al, Nb, Ti, V)-rich oxides with many pores and cracks. Interestingly, a very thin Al_2O_3 layer was found between the outer and inner layers, as shown in Fig. 12c. According to the chemical composition (Table 4), this dense layer consists of (Al, Nb, V)-containing TiO_2. The thermodynamic calculations suggest a layer composed of corundum-type $(Al, V)_2O_3$, Nb_2O_5, rutile-type TiO_2, VO_2, and $V_2O_{5(liq)}$, as shown in Fig. 15. In addition, bright, high atomic number particles exhibited high concentrations of Hf, possibly as a MO_2-type oxide. This HfO_2 was precipitated as separate areas in the oxide layers and tended to be more abundant and coarser in the region closer to the outer layer.

Figure 13 shows the oxide layer formed on the Al_1 alloy after exposure at 900 °C for 9 h. A very thin outer layer consisting of a needle-like (V, Y)-rich oxide, similar to the morphology formed at 800 °C, was found. However, it appears that the (V, Y)-rich oxide layer was less favorable to form than a new (Al, Nb, Ti)-rich oxide layer. Based on Fig. 1, the needle-like structure may provide better spallation resistance than the mixed oxide formed at 700 °C, although it is structurally very brittle and prone to cracking. However, the newly formed oxide layer provides a better spallation resistance, due to the denser structure of the (Al, Nb, Ti)-rich oxide layer.

Figure 14 shows that the needle-like (V, Y)-rich oxide morphology was also found in the $Al_{1.25}$ alloy. In this alloy, both the needle-like (V, Y)-rich oxide and the (Al, Nb, Ti, V)-rich oxide appear thicker than the oxides found on the Al_1 alloy. There were also HfO_2 particles among the needle-like structures, indicating external oxidation of the V and Y to form (V, Y)-oxide scales. The higher Al content appears to affect the formation and stability of the (V, Y)-oxide layer and the (Al, Nb, Ti)-oxide layer underneath.

Discussion

The Oxide Layers

The standard Gibbs energies of formation of Y_2O_3, HfO_2, and Al_2O_3 are the most negative compared to other oxides, as shown in Fig. 16. Even so, oxides of elements that are present in the studied RHEAs possess similar thermodynamic stabilities, but their oxides do not form solid solutions [38]. Therefore, it is expected that the mixture of non-protective oxides will be more favorable than the selective oxidation of protective oxide-forming elements. Note that a non-protective oxide refers to an oxide scale with a linear growth rate and an insufficiently dense morphology, while a protective oxide refers to an oxide scale with a parabolic growth rate and a dense morphology.

The significant weight loss, as shown in Fig. 1, can be explained by the large (and growing) molar volume of the oxide when it oxidizes from a lower oxide (transient oxidation stage) to the higher (final oxidation stage) and the formation of liquid or volatile oxides of V_2O_5 at temperatures higher than 678 °C [19]. They prevent the

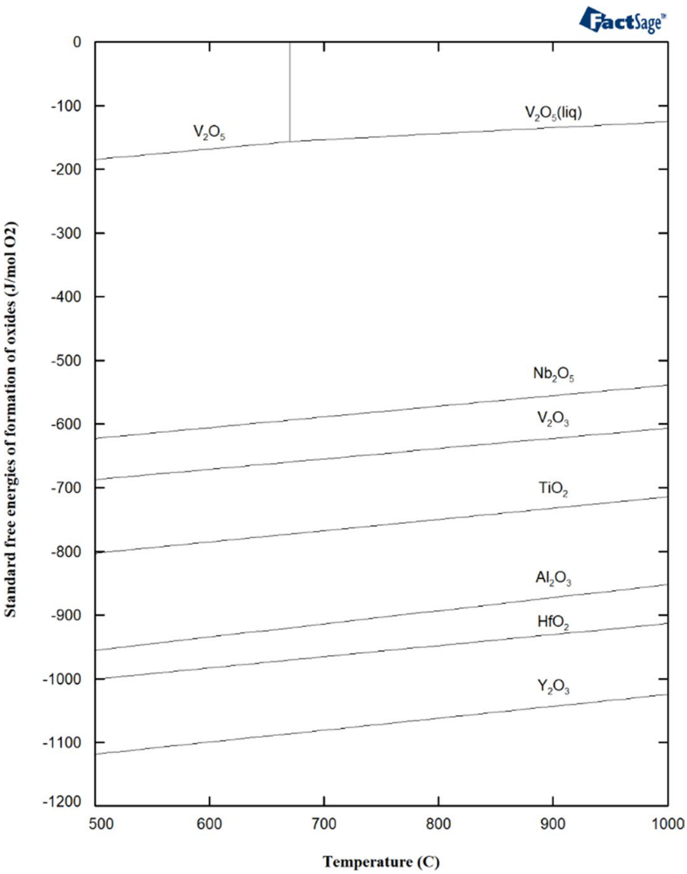

Fig. 16 Calculated thermodynamic stabilities of relevant oxides in this work obtained using the FactSage 8.2 (FactPS and FToxid databases)

formation of dense layers or destroy the integrity of initially protective oxide layers, leading to catastrophic oxidation. The evaporation of volatile V_2O_5 oxides causes the appearance of multiple pores within the V-rich oxide scales, which act as sites for accelerated inward diffusion of oxygen.

It is interesting to note that the morphology and phase composition of the inner and outer layers change at elevated temperatures from one alloy to another (see Figs. 4, 5, 6, 8, 9, 10, 11, 12, 13, 14). A structural evolution of the outer oxide scale occurs in the $Al_{0.75}$ and Al_1 alloys at 800 °C. It significantly improves the pesting and spallation resistance of the $Al_{0.75}$ and Al_1 alloys. The outermost oxide layer is mainly composed of needle-like (V, Y)-rich oxide particles and a (Al, Nb, Ti, V)-rich oxide layer. Their morphologies were similar to those found in $AlNbTiVZr_{0.25}$ HEA [37]. According to Yurchenko [37], the (Al, Nb, Ti, V)-rich oxides can be identified as mixtures of the $TiNb_2O_7$, $AlNbO_4$, and VO_2 oxides. It is known that the formation of the $TiNb_2O_7$ and/or $AlNbO_4$ decrease the oxidation resistance [39–41]. The complex $TiNb_2O_7$ was most likely formed by solid-state reaction between Nb_2O_5 and TiO_2 [37, 39, 42]. The growth of the fast-growing $AlNbO_4$ oxide required Nb ions [43]. The activity of Nb in the oxide layer decreases with the $AlNbO_4$ formation, and the growth of $AlNbO_4$ occurred until the Al activity required to form α-Al_2O_3 was reached. This resulted in α-Al_2O_3 precipitating under the mixed $AlNbO_4$ and $TiNb_2O_7$ oxides as shown in Figs. 8, 9, 13, and 14. Similar morphologies were also found in $Al_{1.25}$ alloy at 900 °C. It appears that a higher Al content delays the formation of needle-like oxides up to 900 °C, thus improving the oxidation resistance at higher temperature.

The solid-state reaction between Nb_2O_5 and TiO_2 can produce a ternary $TiNb_2O_7$ oxide at TiO_2 saturation. According to literature [39, 44, 45], oxygen diffuses through oxygen vacancies in TiO_2. The addition of Nb^{5+}, which has higher valence than Ti^{4+}, reduces oxygen vacancies and prevents the diffusion of oxygen. Consequently, the oxidation resistance will improve by principle of valence control. However, the largest solubility limit of Nb_2O_5 in TiO_2, according to the TiO_2–Nb_2O_5 phase diagram [46, 47], was about 13.5 mol%. When Nb content in the oxide exceeds the solubility limit, phase separation from TiO_2 to TiO_2 and $TiNb_2O_7$ occurs. Ogawa [45] also confirmed that the Nb diffusion occurred during high-temperature oxidation reaction in Ti alloys contained more than 13%Nb.

Once a thick, dense layer of $TiNb_2O_7$ is formed, oxygen atoms may be supplied from the oxide layer to the alloy. This complex oxide often has a large fraction of oxygen vacancies, allowing oxygen in the air to be absorbed and transported through the oxide to the alloy matrix [23, 48, 49]. There is an excess of Hf below the dense oxide layer and it precipitates in the form of HfO_2 particles during the outward diffusion of the (Ti, Nb)-rich oxide in the outermost layer. During the initial stage of oxidation, transient oxides such as TiO and NbO are formed. As both oxides are p-type semiconductors, the metallic ion of Ti and Nb diffuse outward and become enriched in the outermost layer of the oxide. The outward migration causes the concentration of Hf below the outermost oxide to increase, leading to the precipitation of HfO_2 particles with a gradient concentration profile. As a result, the HfO_2 particles near the dense oxide layer are more abundant and coarser.

It is interesting to note that in addition to the HfO_2 oxides, preferentially precipitated near the outer oxide scale, a thin Al_2O_3 oxide layer is also formed just below the dense outer oxide. From a thermodynamic point of view, Al_2O_3 and HfO_2 oxides show only marginal differences in the standard Gibbs energies of formation. Since oxides with similar thermodynamic stabilities tend to form simultaneously, this eventually leads to the formation of both oxides below the (Al, Nb, V)-containing TiO_2. This phenomenon does not exist at 700 °C, when V_2O_5 evaporation appears to be slower. The evaporation rate of V_2O_5 is significant in the selective oxidation of the $Al_{0.75}$ alloy at 900 °C. Since the long-range diffusion of metallic ions is slow in solids, the evaporation of V_2O_5 leaves masses of atomic scale vacancies that act as channels for the outward diffusion of Ti and Nb ions [23, 37]. It results in the formation of the outermost dense oxide layer. In addition, evaporation also generates pores and cracks deep within the inner oxide layer, which act as channels for continuous inward diffusion of oxygen through the TiO_2 oxide toward the metal alloy. This is in

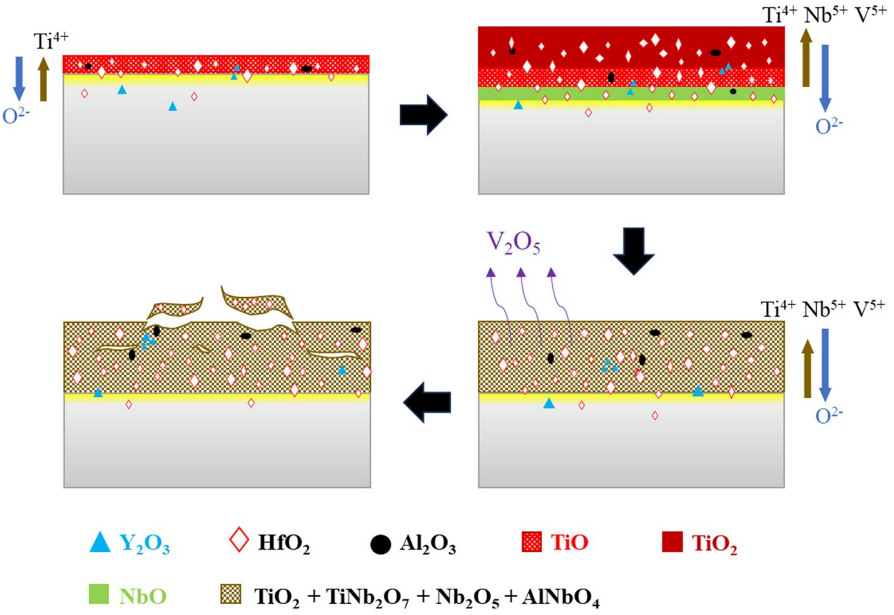

Fig. 17 Schematic illustration of pesting mechanism

agreement with the linear oxidation rate presented in Fig. 2 and Table 3. This mechanism is typically caused by factors such as low vapor pressure and easy evaporation of oxide products as well as instability of the oxide due to high oxygen solubility and transport rates in the matrix [1].

The formation of needle-like (V, Y)-rich oxide scales appears to be effective in retarding the inward diffusion of oxygen at 800 and 900 °C. As shown in Figs. 8, 9, 13, and 14, all alloys with needle-like structures in the outermost oxide scale have few or no pores in the inner oxide layers. Accordingly, pores and cracks were found in the alloys without needle-like oxides.

Thermodynamic calculations, as shown in Fig. 7, indicate that the formation of liquid or volatile oxides of V_2O_5 from other V-oxides requires a higher pO_2 at higher temperatures. This means that the formation of volatile V_2O_5 in the inner oxide layer is much more difficult than in the outermost oxide layer, due to the higher activity of oxygen at the oxide/gas interface. Needle-like morphology seems to indicate that the outward diffusion of the V and Y elements consumes a large amount of oxygen at the air/oxide interface and therefore inhibits the inward diffusion of oxygen into the oxide scale. The slower inward diffusion of oxygen results in low pO_2 in the inner oxide layer, making the formation of V_2O_5 more difficult, and condensed VO_2 is formed instead. Few or no pores were formed in the inner oxide layers. The mixed complex oxides in the inner oxide layers were consistent with the equilibrium calculations and consist of HfO_2, $AlNbO_4$, Nb_2O_5, TiO_2, $TiNb_2O_7$, VO_2, and Y_2O_3.

Oxidation Mechanism

It is crucial to comprehend the mechanism by which the protective oxide layer fails. Understanding the processes found in the SEM observations is essential, as the pesting, bulky oxide formation, as well as the adhesion and spallation behaviors of an oxide layer define its protective features in oxidizing atmospheres.

The analysis of the oxidation behavior on the studied RHEAs leads us to conclude that the oxidation mechanism is influenced by accelerated internal oxidation, as reported by Sheikh et al. [21], followed by the formation of fast-growing non-protective complex oxides. Figure 17 shows a schematic illustration of pesting mechanism on $Al_xHfNbTiVY_{0.05}$ RHEAs in agreement with the experimental results. At the initial stage of oxidation, the oxide phase appears to contain a large fraction of HfO_2, in which all other alloying elements are insoluble, some Al_2O_3 precipitates, and a small fraction of Y_2O_3. The MO-type of oxides is thermodynamically the most stable stoichiometry for Ti, V, and Nb as evaluated by Wei et al. [13] and Jacob et al. [50]. Therefore, the formation of MO-type oxides will be the other part of the oxide scales with Ti being the dominant element. The formation of MO-type oxides during the initial stage of oxidation does not dissolve much oxygen but generates higher oxides on the outermost of the scales, thus increasing the molar volume of the scales.

TiO has a large number of vacancies on both the titanium and oxygen sublattices [51]. The concentration of Ti vacancies in TiO is higher than that of O vacancies. Thus, Ti ion diffuses faster in TiO and is oxidized on the outer surface to form a stoichiometric layer of TiO_2. Stone et al. [52] suggested that interstitial Ti ions play an active role in the outward growth of TiO_2. Since TiO_2 has a high concentration of oxygen vacancies, inward diffusion of oxygen is favored, allowing oxygen to react with other elements in the alloys to form other oxides, such as NbO and VO. The formation of NbO, which has high concentrations of cation vacancies, allows outward diffusion of Nb at the substrate/NbO interface. Oxygen inward diffusion at the TiO_2/NbO interface and Nb outward diffusion at the substrate/NbO interface occur simultaneously, allowing the formation of Nb_2O_5. When Nb_2O_5 exceeds the solubility limit of TiO_2, $TiNb_2O_7$ is precipitated. Once a thick oxide layer is formed, oxidation proceeds at the oxide/substrate interface and inward diffusion of oxygen becomes dominant. The excess of Nb_2O_5 may also react with Al_2O_3 to form fast-growing $AlNbO_4$ as described by Tolpygo et al. [29].

The formation of TiO_2, $TiNb_2O_7$, and fast-growing, porous oxides, such as $AlNbO_4$, allow inward diffusion of oxygen. The diffused oxygen is absorbed by oxide growth and dissolution in the alloy. While the fast-growing outer scale grows, internal oxidation occurs according to the specific diffusion coefficients of oxygen in a given alloy. Therefore, the pesting behavior at 700 °C is expected to correlate with the formation of the mixed oxides Nb_2O_5, $TiNb_2O_7$, and $AlNbO_4$. The crucial point for the formation of the complex oxides $TiNb_2O_7$ and $AlNbO_4$ is that Nb_2O_5—as a precursor for the formation of both $AlNbO_4$ and $TiNb_2O_7$—has several polymorphic structures. The formation of bulky oxide may correlate with the formation of β-Nb_2O_5, which has a significant volume expansion when transformed from α-Nb_2O_5 [53]. In addition, the Nb_2O_5 oxide has an extremely high PBR (2.66) compared to its transient oxide counterparts, e.g., NbO (PBR = 1.38) and NbO_2 (PBR = 1.95), which results in high compressive stress in the growing oxide scale [14], leading to its continuous cracking and spallation.

At 800 and 900 °C, the oxidation mechanism appears to change to the formation of VO_2 within the oxide scale, which is more desirable than the formation of volatile V_2O_5. This reduces the number of pores due to the lack of V_2O_5 evaporation. However, internal oxidation will still occur because most of the forming oxide scales, e.g., Nb_2O_5, VO_2, TiO_2, $AlNbO_4$, have a semiconducting nature with a high concentration of oxygen vacancies. Oxygen vacancies, interpreted as n-type conductivity, act as electron donors that accelerate the transfer of oxygen from the gas to the base alloy. Nevertheless, outward diffusion of the V and Ti atoms is still more likely to occur. The smaller, lighter V atoms can still migrate rapidly to the surface of the oxide, forming needle-like (V, Y)-rich oxide scales.

Effect of Aluminum

In terms of pesting and spallation resistance, $Al_{1.25}$ alloy shows an advantage over the less Al-containing alloys at 700 °C. The multiple mixed oxides that are forming on high Al-containing RHEA provide a better protection than the double layer oxide scales that are forming in less Al-containing RHEA. Similar to the Al_xHfNbTaTiZr system [22], the heat of formation of alumina in the Al_xHfNbTiV$Y_{0.05}$ system is only slightly different from that of hafnium, zirconium, and yttrium oxide, but more negative than that of the other oxides. The distribution of such heat of formation or the diffusivity of the constituent elements causes a competition between alumina formation and oxide growth. In addition, the structures of Al_2O_3 and the other oxides are different, which makes the formation of oxide solid solution hard. This means that the solubilities of the oxides in dense Al_2O_3 are low because some oxides are 4-valent (Hf, Ti, Zr) and some even 5-valent (Nb, Ta). As a result, the oxide layer consists of a mixture of different oxide phases. The low Al content does not help much in overcoming pesting, because the small amount of Al would dissolve during transient oxidation, resulting in even worse oxidation resistance [54]. Nevertheless, the mixed oxides are still not dense enough to protect against oxidation and exhibit many cracks because the formation of higher oxides introduces large lattice distortions and stresses. Therefore, severe spallation will occur after prolonged exposure as the cracks develop further.

At 800 °C, $Al_{0.75}$ alloy has better spallation resistance and shows the formation of thin needle-like oxides on the outermost layer and dense mixed oxides on the inner layer. On the other hand, alloys with higher Al content show more severe spallation due to the formation of a single but porous non-protective mixed oxide layer. Interestingly, continuous weight gains occurred in all alloys at 900 °C and no spallation was found. The weight gain in the $Al_{0.75}$ and $Al_{1.25}$ alloys followed a near-linear growth rate; while, the Al_1 alloy followed near-parabolic growth kinetics. The structural evolution of the oxide in non-equiatomic Al-containing alloys affects oxidation

Table 5 Parabolic rate constants for $Al_xHfNbTiVY_{0.05}$, NiAl, and FeCrAl

Materials	Technique	Temperature (°C)	k_p (g^2/cm^4 s)	Sources
$Al_{0.75}HfNbTiVY_{0.05}$	Arc melting	800	7.9×10^{-10}	Present work
$Al_1HfNbTiVY_{0.05}$	Arc melting	800	1.5×10^{-10}	Present work
$Al_1HfNbTiVY_{0.05}$	Arc melting	900	1.1×10^{-9}	Present work
NiAl	Arc melting	800	5.9×10^{-14}	[55]
NiAl	Arc melting	1100	3.6×10^{-12}	[56]
FeCrAl	Arc melting	1100	3.2×10^{-12}	[57]

growth rates, particularly at lower Al content, where the kinetics changed from near-parabolic to near-linear at higher temperatures.

Table 5 lists the parabolic rate constants (k_p, g^2/cm^4 s) of $Al_xHfNbTiVY_{0.05}$ alloys compared to typical alumina-forming alloys at various temperatures. The k_p values are orders of magnitude higher than those of NiAl and FeCrAl alloys, indicating poor oxidation resistance of these alloys. Some of the *k* values for the studied alloys are not included in this table due to their near-linear growth rates.

In general, despite the poor oxidation resistance of the $Al_xHfNbTiVY_{0.05}$ alloy, the results obtained show that higher Al content can provide a better protection against pesting at 700 °C. Detailed characterization of the oxide scales shows that the presence of Nb_2O_5 contributes to the formation of voluminous, fast-growing oxides that allow oxygen to diffuse inward and further lead to macroscopic catastrophic oxidation. In addition, the partial evaporation of V_2O_5 is believed to contribute to accelerating the disintegration of oxide scales. The reduction of Nb and V concentrations is believed to be an important factor in improving the oxidation resistance of AlHfNbTiV-type RHEAs.

Conclusions

The oxidation behavior and mechanisms of Y-doped $Al_xHfNbTiV$ refractory high-entropy alloys at 700–900 °C were investigated in this work. Based on the obtained results and analysis, the following conclusions can be drawn:

(1) At 700 °C, all the alloys studied show disintegration by pesting. This has been attributed to the accelerated internal oxidation followed by spallation of the oxide scale due to the formation of voluminous Nb_2O_5, $TiNb_2O_7$, and fast-growing $AlNbO_4$, and is thought to be related to partial evaporation of V_2O_5. The thermodynamic calculations are in reasonable agreement with the experimental results and show that the oxide layers are composed of mixed complex oxides HfO_2, corundum-type $(Al, V)_2O_3$, Nb_2O_5, rutile-type TiO_2, $V_2O_{5(liq)}$, and Y_2O_3.

(2) Transitions in the oxidation mechanism occurred at 800 °C. The structural evolution of the oxide layer formation significantly improves the pesting and spallation resistance of studied $Al_{0.75}$ and Al_1 alloys. The formation of needle-like (V, Y)-

rich oxide particles and a (Al, Nb, Ti, V)-rich oxide layer prevents the outward diffusion of metallic cations.

(3) The formation of dense (V, Y)-rich oxides in the outermost oxide scale retards the inward diffusion of oxygen. However, it cannot completely prevent the continuous inward diffusion of oxygen from the surrounding air. The formation of a mixture of the complex needle-like (V, Y)-rich oxide particles and an (Al, Nb, Ti, V)-rich oxide layer was found in the Al_1 alloy. The same oxidation mechanism occurred at 900 °C.

(4) A higher Al content may provide better protection against accelerated oxidation and pesting disintegration at 700 °C. The oxidation rate also changes from a near-linear to a near-parabolic at 900 °C. However, the higher Al content showed a drawback at the transition from lower to higher temperatures due to the evolution of the oxide layers at this temperature.

Acknowledgements The financial support of the ITB International Research Program 2022, grant no. LPPM.PN-10-34-2022 is gratefully acknowledged. A part of this work was carried out at the Thermodynamics and Modelling Research Group of the Department of Chemical and Metallurgical Engineering, School of Chemical Engineering, Aalto University. This work utilized the Academy of Finland's RawMatTERS Finland Infrastructure (RAMI) based at Aalto University, GTK Espoo, and VTT Espoo.

Author Contributions F.M. contributed to conceptualization, investigation, methodology, software, data curation, writing—original draft and editing. D.S. contributed to methodology, validation, and writing—review. L.K. contributed to methodology, validation, writing—review and editing. D.S. was involved in methodology, validation, writing—review and editing. E.A.B contributed to methodology, supervision, validation, funding acquisition, and writing—review. D.L. contributed to methodology, software, supervision, validation, and writing—review. P.T. contributed to methodology, supervision, validation, writing—review and editing. All other authors reviewed the manuscript.

Declarations

Conflict of interest The authors declare that they have no competing financial interests or personal relationships that could have appeared to influence the work reported in this paper.

References

1. O. N. Senkov, S. V. Senkova, D. M. Dimiduk, C. Woodward, and D. B. Miracle, *Journal of Materials Science* **47**, 6522 (2012). https://doi.org/10.1007/s10853-012-6582-0.
2. T. M. Pollock and S. Tin, *Journal of Propulsion and Power* **22**, 361 (2006). https://doi.org/10.2514/1.18239.
3. Y. Yan, K. A. McGarrity, D. J. Delia, C. Fekety, and K. Wang, *Corrosion Science* **204**, 110377 (2022). https://doi.org/10.1016/j.corsci.2022.110377.
4. R. A. MacKay, T. P. Gabb, J. L. Smialek, and M. V. Nathal, *Alloy Design Challenge : Development of Low Density Superalloys for Turbine Blade Applications*. (NASA TM 2009-215819, 2009), p. 1.
5. J. W. Yeh, S. K. Chen, S. J. Lin, J. Y. Gan, T. S. Chin, T. T. Shun, et al., *Advanced Engineering Materials* **6**, 299 (2004). https://doi.org/10.1002/adem.200300567.
6. B. Cantor, I. T. H. Chang, P. Knight, and A. J. B. Vincent, *Materials Science and Engineering A* **375–377**, 213 (2004). https://doi.org/10.1016/j.msea.2003.10.257.
7. O. N. Senkov, G. B. Wilks, J. M. Scott, and D. B. Miracle, *Intermetallics* **19**, 698 (2011). https://doi.org/10.1016/j.intermet.2011.01.004.

8. O. N. Senkov, J. M. Scott, S. V. Senkova, D. B. Miracle, and C. F. Woodward, *Journal of Alloys and Compounds* **509**, 6043 (2011). https://doi.org/10.1016/j.jallcom.2011.02.171.
9. O. N. Senkov, G. B. Wilks, D. B. Miracle, C. P. Chuang, and P. K. Liaw, *Intermetallics* **18**, 1758 (2010). https://doi.org/10.1016/j.intermet.2010.05.014.
10. O. N. Senkov and C. F. Woodward, *Materials Science and Engineering A* **529**, 311 (2011). https://doi.org/10.1016/j.msea.2011.09.033.
11. O. N. Senkov, S. V. Senkova, D. B. Miracle, and C. Woodward, *Materials Science and Engineering A* **565**, 51 (2013). https://doi.org/10.1016/j.msea.2012.12.018.
12. Z. Lei, X. Liu, Y. Wu, H. Wang, S. Jiang, S. Wang, et al., *Nature* **563**, 546 (2018). https://doi.org/10.1038/s41586-018-0685-y.
13. S. Wei, S. J. Kim, J. Kang, Y. Zhang, Y. Zhang, T. Furuhara, et al., *Nature Materials* **19**, 1175 (2020). https://doi.org/10.1038/s41563-020-0750-4.
14. B. Gorr, S. Schellert, F. Müller, H. J. Christ, A. Kauffmann, and M. Heilmaier, *Advanced Engineering Materials* (2021). https://doi.org/10.1002/adem.202001047.
15. B. Gorr, F. Müller, M. Azim, H. J. Christ, T. Müller, H. Chen, et al., *Oxidation of Metals* **88**, 339 (2017). https://doi.org/10.1007/s11085-016-9696-y.
16. T. M. Butler and K. J. Chaput, *Journal of Alloys and Compounds* **787**, 606 (2019). https://doi.org/10.1016/j.jallcom.2019.02.128.
17. O. A. Waseem, U. Auyeskhan, H. M. Lee, and H. J. Ryu, *Journal of Materials Research* **33**, 3226 (2018). https://doi.org/10.1557/jmr.2018.241.
18. K. C. Lo, H. Murakami, J. W. Yeh, and A. C. Yeh, *Intermetallics* **119**, 106711 (2020). https://doi.org/10.1016/j.intermet.2020.106711.
19. C. M. Liu, H. M. Wang, S. Q. Zhang, H. B. Tang, and A. L. Zhang, *Journal of Alloys and Compounds* **583**, 162 (2014). https://doi.org/10.1016/j.jallcom.2013.08.102.
20. T. Maruyama and K. Yanagihara, *Materials Science and Engineering A* **239–240**, 828 (1997). https://doi.org/10.1016/s0921-5093(97)00673-4.
21. S. Sheikh, M. K. Bijaksana, A. Motallebzadeh, S. Shafeie, A. Lozinko, L. Gan, et al., *Intermetallics* **97**, 58 (2018). https://doi.org/10.1016/j.intermet.2018.04.001.
22. C. H. Chang, M. S. Titus, and J. W. Yeh, *Advanced Engineering Materials* **20**, 1 (2018). https://doi.org/10.1002/adem.201700948.
23. D. Ouyang, Z. Chen, H. Yu, K. C. Chan, and L. Liu, *Corrosion Science* **198**, 110153 (2022). https://doi.org/10.1016/j.corsci.2022.110153.
24. F. Muhammad, E. A. Basuki, A. A. Korda, Z. Zulhan, and D. H. Prajitno, *Journal of Non-Crystalline Solids* **613**, 122392 (2023). https://doi.org/10.1016/j.jnoncrysol.2023.122392.
25. C. W. Bale, E. Bélisle, P. Chartrand, S. A. Decterov, G. Eriksson, A. E. Gheribi, et al., *Calphad* **54**, 35 (2016). https://doi.org/10.1016/j.calphad.2016.05.002.
26. O. N. Senkov, D. B. Miracle, K. J. Chaput, and J. P. Couzinie, *Journal of Materials Research* **33**, 3092 (2018). https://doi.org/10.1557/jmr.2018.153.
27. Y. K. Mu, Y. D. Jia, L. Xu, Y. F. Jia, X. H. Tan, J. Yi, et al., *Materials Research Letters* **7**, 312 (2019). https://doi.org/10.1080/21663831.2019.1604443.
28. M. K. Meyer and M. Akinc, *Journal of the American Ceramic Society* **79**, 938 (1996). https://doi.org/10.1111/j.1151-2916.1996.tb08528.x.
29. V. K. Tolpygo and H. J. Grabke, *Scripta Metallurgica et Materiala* **28**, 747 (1993). https://doi.org/10.1016/0956-716X(93)90047-V.
30. T. C. Chou and T. G. Nieh, *Journal of Materials Research* **8**, 214 (1993). https://doi.org/10.1557/JMR.1993.0214.
31. J. H. Westbrook and D. L. Wood, *Journal of Nuclear Materials* **12**, 208 (1964). https://doi.org/10.1016/0022-3115(64)90142-4.
32. P. J. Meschter, *Metallurgical Transactions A* **23**, 1763 (1992). https://doi.org/10.1007/BF02804369.
33. C. G. McKamey, P. F. Tortorelli, J. H. DeVan, and C. A. Carmichael, *Journal of Materials Research* **7**, 2747 (1992). https://doi.org/10.1557/JMR.1992.2747.
34. D. A. Berztiss, R. R. Cerchiara, E. A. Gulbransen, F. S. Pettit, and G. H. Meier, *Materials Science and Engineering: A* **155**, 165 (1992). https://doi.org/10.1016/0921-5093(92)90324-T.
35. G. Mi, K. Yao, P. Bai, C. Cheng, and X. Min, *Metals (Basel)* **7**, 226 (2017). https://doi.org/10.3390/met7060226.
36. M. Esmaily, Y. Qiu, S. Bigdeli, M. B. Venkataraman, A. Allanore, and N. Birbilis, *npj Materials Degradation* **4**, 25 (2020). https://doi.org/10.1038/s41529-020-00129-2.

37. N. Yurchenko, E. Panina, S. Zherebtsov, G. Salishchev, and N. Stepanov, *Oxidation Materials* **11**, 2526 (2018). https://doi.org/10.3390/ma11122526.
38. A. S. Gandhi and C. G. Levi, *Journal of Materials Research* **20**, 1017 (2005). https://doi.org/10.1557/JMR.2005.0133.
39. H. Jiang, M. Hirohasi, Y. Lu, and H. Imanari, *Scripta Materialia* **46**, 639 (2002). https://doi.org/10.1016/S1359-6462(02)00042-8.
40. C. Leyens, *Journal of Materials Engineering and Performance* **10**, 225 (2001). https://doi.org/10.1361/105994901770345259.
41. A. Ralison, F. Dettenwanger, and M. Schütze, *Materials and Corrosion* **51**, 317 (2000). https://doi.org/10.1002/(SICI)1521-4176(200005)51:5%3c317::AID-MACO317%3e3.0.CO;2-W.
42. S. C. Parida, N. K. Gupta, K. Krishnan, G. A. Rama Rao, and B. K. Sen, *Metallurgical and Materials Transactions A* **39**, 2020 (2008). https://doi.org/10.1007/s11661-008-9548-8.
43. V. Gauthier, C. Josse, J. P. Larpin, and M. Vilasi, *Oxidation of Metals* **54**, 27 (2000). https://doi.org/10.1023/a:1004694327812.
44. P. Pérez, V. A. C. Haanappel, and M. F. Stroosnijder, *Materials Science and Engineering: A* **284**, 126 (2000). https://doi.org/10.1016/S0921-5093(00)00754-1.
45. Y. Ogawa and E. Miura-Fujiwara, *Materials Transactions* **60**, 2204 (2019). https://doi.org/10.2320/matertrans.MT-M2019136.
46. C. Liu, P. Luo, Y. Feng, W. Gong, and F. Zhang, *Ceramics International* **49**, 30471 (2023). https://doi.org/10.1016/j.ceramint.2023.06.311.
47. R. S. Roth, *Progress in Solid State Chemistry* **13**, 159 (1980). https://doi.org/10.1016/0079-6786(80)90003-5.
48. N. Birks, G. H. Meier, and F. S. Pettit, *Introduction to the High Temperature Oxidation of Metals*, 2nd ed (Cambridge University Press, Cambridge, 2006), https://doi.org/10.1017/CBO9781139163903.
49. E. M. Savitskii and G. S. Burkhanov, *Physical Metallurgy of Refractory Metals and Alloys*, (Springer US, 1995). https://doi.org/10.1007/978-1-4684-1572-8.
50. K. T. Jacob, C. Shekhar, M. Vinay, and Y. Waseda, *Journal of Chemical and Engineering Data* **55**, 4854 (2010). https://doi.org/10.1021/je1004609.
51. P. M. Woodward, P. Karen, J. S. O. Evans, and T. Vogt, *Solid State Materials Chemistry*, (Cambridge University Press, 2021). https://doi.org/10.1017/9781139025348.
52. P. Stone, R. A. Bennett, and M. Bowkery, *New Journal of Physics* 1999. https://doi.org/10.1088/1367-2630/1/1/008.
53. B. Voglewede, V. R. Rangel, and S. K. Varma, *Corrosion Science* **61**, 123 (2012). https://doi.org/10.1016/j.corsci.2012.04.029.
54. L. Korb and D. Olson, *ASM Metals Handbook: Corrosion*, vol. 13. (ASM international, 1992),.
55. G. Geramifard, C. Gombola, P. Franke, and H. J. Seifert, *Corrosion Science* **177**, 108956 (2020). https://doi.org/10.1016/j.corsci.2020.108956.
56. B. A. Pint, K. L. More, and I. G. Wright, *Oxidation of Metals* **59**, 257 (2003). https://doi.org/10.1023/A:1023087926788.
57. B. A. Pint, *Journal of the American Ceramic Society* **86**, 686 (2003). https://doi.org/10.1111/j.1151-2916.2003.tb03358.x.

Authors and Affiliations

Fadhli Muhammad[1,2,3] · Dmitry Sukhomlinov[3] · Lassi Klemettinen[3] · David Sibarani[3] · Eddy Agus Basuki[2] · Daniel Lindberg[3] · Pekka Taskinen[3] · Akhmad Ardian Korda[2] · Zulfiadi Zulhan[2] · Djoko Hadi Prajitno[4]

✉ Fadhli Muhammad
fadhlim_08@itb.ac.id

Dmitry Sukhomlinov
dmitry.sukhomlinov@aalto.fi

Lassi Klemettinen
lassi.klemettinen@aalto.fi

David Sibarani
david.sibarani@aalto.fi

Eddy Agus Basuki
eddy.a.basuki@itb.ac.id

Daniel Lindberg
daniel.k.lindberg@aalto.fi

Pekka Taskinen
pekka.taskinen@aalto.fi

Akhmad Ardian Korda
korda@itb.ac.id

Zulfiadi Zulhan
zulfiadi.zulhan@itb.ac.id

Djoko Hadi Prajitno
djok003@brin.go.id

1 Doctorate Program of Mining Engineering, Faculty of Mining and Petroleum Engineering, Institut Teknologi Bandung, Jl. Ganesha 10, Bandung, Jawa Barat 40132, Indonesia

2 Department of Metallurgical Engineering, Faculty of Mining and Petroleum Engineering, Institut Teknologi Bandung, Jl. Ganesha 10, Bandung, Jawa Barat 40132, Indonesia

3 Department of Chemical and Metallurgical Engineering, School of Chemical Engineering, Aalto University, Kemistintie 1F, P.O. Box 16100, 00076 Aalto, Finland

4 Nuclear Research Center, National Research and Innovation Agency, Jl. Tamansari 71, Bandung, Jawa Barat 40132, Indonesia